Correlation of Hybrid Rocket Propellant Regression Measurements with Enthalpy-Balance Model Predictions

Shannon D. Eilers.
Utah State University, 4130 Old Main Hill, Logan, UT, 84322-4130

An enthalpy-balance fuel-grain regression model is presented. The regression model, based on the longitudinally averaged fuel recession rates, is shown to accurately predict the chamber pressure, thrust and specific impulse performance of small and medium scale hybrid rocket motors. The key to the model predictions is the longitudinal enthalpy balance between the fuel grain heat of ablation and the convective heat transfer from the flame zone to the model surface. Convective heat transfer is related to the surface skin friction using the Reynolds analogy for turbulent flow. Simple flat plate models are used to predict the longitudinally averaged skin friction coefficient. Chemical properties of the combustion products were evaluated using the NASA Computer Equilibrium with Applications (CEA) Combustion code. Model predictions for a nitrous oxide (N_2O) and hydroxyl-terminated poly butadiene (HTPB) motor are compared to data from a small-scale test firing with a 4-inch diameter motor. Suggestions for model improvements are offered.

Nomenclature

A^*	=	nozzle throat area	$\dot{r}$	=	instantaneous regression rate
A_{burn}	=	total surface area	Re_L	=	Reynolds number
$A_{c_{\text{chamber}}}$	=	chamber cross sectional area	R_g	=	gas constant
A_{ox}	=	injector hole area	S_t	=	Stanton number
$C_{d_{ox}}$	=	injector discharge coefficient	t	=	time
C_f	=	longitudinally averaged c_f coefficient	T_0	=	stagnation temperature
c_{fx}	=	local skin friction coefficient	T_{flame}	=	flame temperature
c_p	=	solid fuel specific heat	T_{fuel}	=	fuel temperature
c_{p_e}	=	specific heat of oxidizer at flame	U_e	=	oxidizer velocity at flame boundary
D_H	=	hydraulic diameter	V_c	=	combustion chamber volume
H	=	convective heat transfer coefficient	δ	=	Boundary layer thickness
h_v	=	heat of vaporization	$\Delta h_{\text{surface}}$	=	temperature difference at fuel surface
L	=	length of fuel grain	γ	=	specific heat ratio
$\dot{m}_{\text{fuel}}$	=	mass flow rate of fuel	μ_{ox}	=	oxidizer viscosity
$\dot{m}_{ox}$	=	mass flow rate of oxidizer	ρ_{fuel}	=	fuel density
$\dot{m}_{\text{propellant}}$	=	mass flow rate of propellant	ρ_{ox}	=	oxidizer density
M_R	=	instantaneous mixture ratio	τ_{wall}	=	wall shear stress
p_0	=	stagnation pressure	$(c_{fx})_{\text{blowing}}$	=	c_f coefficient with blowing adjustment
p_{ox}	=	oxidizer pressure			
P_r	=	Prandtl number			
$\dot{q}$	=	total heat transfer at surface			

I. Introduction

Almost seventy per cent of all the catastrophic rocket-system failures are attributable to the power-plant of the rocket.[1] Reduction of the probability of propulsion failures requires picking the right rocket engine type. There are three major types of rocket engines. Liquid propellant engines use an oxidizer and a separate fuel that is mixed through injectors within the combustion chamber. Solid propellant motors use a solid propellant grain that contains both the oxidizer and the fuel. A hybrid motor typically uses a liquid oxidizer such as nitrous oxide or liquid oxygen and a separate solid fuel grain such as rubber or plastic.

Both liquid rocket engines and solid rocket motors can catastrophically explode. For example, the estimate for the Space Shuttle's liquid fueled main engines is one explosion every 1530 sorties per engine and for its solid rocket boosters, one explosion every 1550 sorties per motor. Hence designers limit the number of such engines to reduce the possibility of explosion. A large number of liquid engines or solid motors increase the chance of a catastrophic failure. On the other hand, according to the US Department of Transportation, [2] hybrid motors can be fabricated, stored, and operated without any possibility of explosion or detonation. Other advantages of Hybrid Rockets include the ability to be stopped, restarted, and throttled; easy (and hence potentially cheaper) ground handling; and relative insusceptibility to grain flaws. Multiple hybrid motors can be used to improve propulsion system reliability by providing redundancy in the case that one hybrid motor fails to produce adequate thrust

A large Hybrid Motor built by Space Development Corporation (San Diego, CA) powered the Scaled Composites Spaceship One® to the first privately funded manned-spaceflights, and the eventual X-prize championship. The future of privately funded manned space flight will be closely tied to the improvement, characterization, and development of hybrid rocket systems. A typical hybrid motor layout is depicted in Fig. 1.[3] The relative positions of the oxidizer tank, pressurant tank, fuel chamber, and nozzle depend on the specific motor design. Some designs rely on the natural vapor pressure of the oxidizer to feed the injector and the pressurant tank is eliminated from the design altogether.

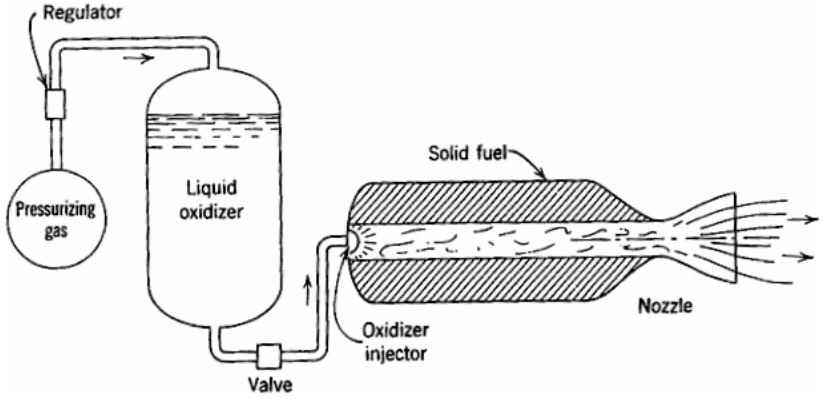

Figure 1. Typical hybrid motor hardware layout.

The advantages of hybrid technology, however, also come with their own set of technological challenges. Prominent among these challenges is the characterization of regression rate scaling effects. Hybrid rocket technology is still a developing field that makes small-scale tests of potential fuel combinations invaluable to the development of hybrid propulsion systems. However, hybrid motor combustion parameters are complex and the scaling effects of regression rate and burn pattern are still not well understood. Some research has been done in an attempt to establish similarity conditions for small-scale firings with full-scale counterparts, but this research has primarily involved testing of only very small lab scale motors. Extrapolation of these parameters to actual flight scale hybrid motors is difficult and mistakes can be costly.

Currently, industry uses an empirical curve fit approach to determine the fuel regression rate[4,5], but this method requires multiple tests of a given fuel or grain configuration to determine the coefficients. Additionally, these relations do little to aid in the prediction of performance of new fuel formulations or grain designs. This paper develops a better model for predicting the motor recession rates using an enthalpy-balance where the ablation heat of the fuel grain is balanced by the convective heat transfer from the combustion flame zone to the fuel grain surface. The recession model, based on the longitudinally averaged fuel recession rates, is shown to accurately predict the chamber pressure, thrust and specific impulse performance of small and medium scale hybrid rocket motors.

II. Enthalpy-Based Model Development

Sutton and Biblarz outline the basic structure of the enthalpy-balance regression rate model used for this analysis.[6] For this model it is assumed that a turbulent flame zone close to the fuel surface dominates combustion in hybrid rocket motors. Boundary layer mixing creates a region where oxidizer flow from the center of the motor combustion port mixes with vaporizing solid fuel leaving the fuel wall. Close to the fuel wall is the flame zone where the combustion of fuel and oxidizer primarily takes place. Heat transfer from this zone to the solid fuel grain drives the regression rate behavior of hybrid rocket motors. This process is depicted in Fig. 2.

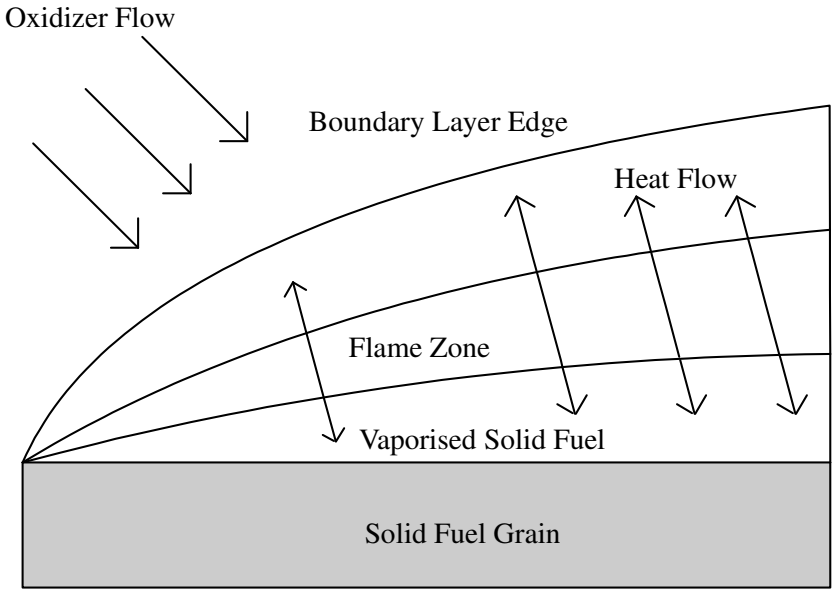

Figure 2 Flame zone typical to hybrid rocket combustion.

The enthalpy-based regression model starts with the examination of heat transfer in a control unit on the fuel grain surface. Heat transfer from convection is directly related to the fuel regression rate through

$$\dot{q} = \rho_{\text{fuel}} \dot{r} h_v \,. \tag{1}$$

The heat transfer from convection is equated to the heat transfer across the solid fuel grain at the fuel grain surface. Assuming an approximately cylindrical port geometry, this enthalpy balance gives

$$\rho_{\text{fuel}} \dot{r} h_v = H(T_{\text{flame}} - T_{\text{surface}}) \,. \tag{2}$$

In Eq. 2, $\dot{r}$ is the linear rate of change of the fuel port radius -- equivalent to the rate of fuel grain regression. For a non-cylindrical port geometry, the port radius can be approximated by one-half of the hydraulic diameter, $D_H = (4A_c\pi)^{1/2}$. Figure 3 illustrates the fuel regression for a particular cross section within the motor.

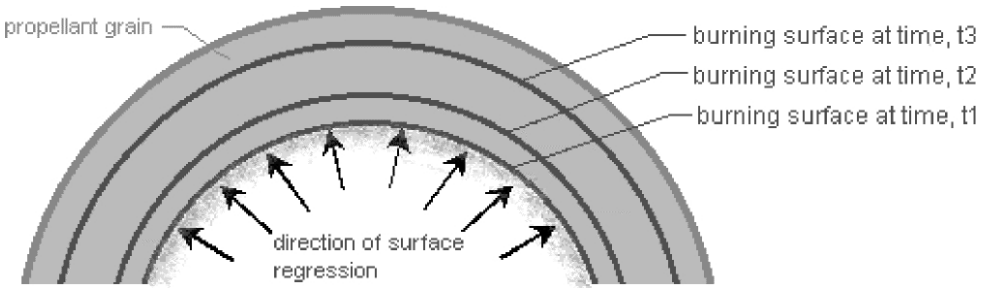

Figure 3. Grain regression in a circular fuel port.

The convective heat transfer coefficient in Eq. 2 is expressed in terms of the Stanton number,

$$H = C_{p_e} \rho_e U_e S_t \,. \tag{3}$$

Equation 3 is substituted into Eq. 2 to give

$$\rho_{\text{fuel}} \dot{r} h_v = S_t \rho_e U_e c_{p_e} (T_{\text{flame}} - T_{\text{surface}}) = S_t \rho_e U_e C_{p_e} \Delta h_{\text{surface}} \,, \tag{4}$$

where U_e, ρ_e, c_{p_e} are the oxidizer velocity, density, and specific heat at the edge of the flame boundary, respectively. The Δh term is the enthalpy difference between the gas at the surface of the fuel grain and the gas within the flame zone. The Stanton number can be related to the local skin friction coefficient and Prandtl number using the Reynold's analogy for turbulent flow with non-unity Prandtl number,[7]

$$S_t = \frac{c_{f_x}}{2} P_r^{-\frac{2}{3}} \,. \tag{5}$$

Because the internal flow in a hybrid motor of this size is highly turbulent, the Prandtl number can be approximated by a constant value of 0.8. This magnitude is selected as a mean value from data presented by Zukauskas and Stanciauskas.[8] Substituting Eq. 5 into Eq. 4 and solving for the recession rate yields

$$\dot{r} = \frac{\left[\frac{c_{f_x}}{2} P_r^{-\frac{2}{3}} \right] \Delta h_{\text{surface}} \rho_e U_e}{\rho_{\text{fuel}} h_v} \,. \tag{6}$$

The Reynolds analogy is strictly valid only for fixed wall boundaries with no out-gassing, and a correction factor for surface blowing is needed to account for the lubricating effect of the vaporized fuel. This correction for a fuel surface that is actively evaporating is presented by Lees[9] as

$$\left(c_{f_x} \right)_{blowing} = 1.27 \left(\frac{\Delta h_{\text{surface}}}{h_v} \right)^{-0.77} c_{f_x} \,. \tag{7}$$

Substituting Eq. 7 into Eq. 6 and collecting terms gives the corrected form of the recession rate equation.

$$\dot{r} = \frac{.635 \left(\frac{\Delta h_{\text{surface}}}{h_v} \right)^{.23} \left[c_{f_x} P_r^{-\frac{2}{3}} \right] \rho_e U_e}{\rho_{\text{fuel}}} \,. \tag{8}$$

Equation 8 is generally valid at each longitudinal point along the fuel grain and clearly the boundary layer within the tube will grow until fully developed channel flow is reached. This boundary layer growth process is depicted in Fig. 4.

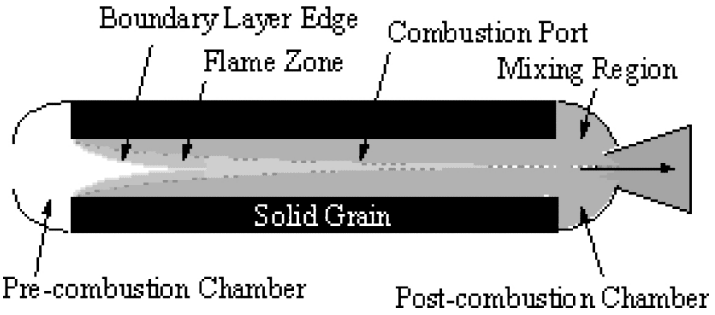

Figure 4. Longitudinal boundary layer development within the fuel port.

The fuel grain geometries under consideration for this model typically have very low aspect ratios with length to diameter ratios less than 20, and fully developed channel flow is not reached until far downstream along the port length. For this analysis, a simple so an empirical skin friction model based on flat plate boundary layer theory was used in lieu of a fully developed model for pipe-flow skin friction. This model was developed based on the empirical relationship for boundary layer thickness,

$$\delta_x = \frac{0.38}{\left(\mathrm{R}_{e_x}\right)^{1/5}} = \frac{0.38}{\left(\frac{\rho U_e x}{\mu}\right)^{1/5}}, \tag{9}$$

and the Blasius formula for turbulent wall shear stress[10]

$$c_{f_x} = \frac{\tau_{wall_x}}{\frac{1}{2}\rho U_e^{\,2}} = \frac{0.0465}{\left(\mathrm{R}_{e_\delta}\right)^{1/4}} = \frac{0.0465}{\left(\frac{\rho U_e \delta_x}{\mu}\right)^{1/4}}, \tag{10}$$

Equations 9 and 10 are valid for $10^6 < \mathrm{Re}_x < 10^7$. Substituting Eq. 9 into Eq. 10 and collecting terms,

$$c_{f_x} = \frac{\tau_{wall}}{\frac{1}{2}\rho U_e^{\,2}} = \frac{0.465}{\left(\frac{\rho U_e}{\mu}\cdot\frac{0.38}{\left(\frac{\rho U_e x}{\mu}\right)^{1/5}}\right)^{1/4}} = \tag{11}$$

$$0.0465\cdot\left(\frac{1}{0.38}\right)^{1/4}\cdot\left(\frac{1}{\left(\frac{\rho U_e}{\mu}\right)^{5/5}\cdot\left(\frac{\rho U_e}{\mu}\right)^{-1/5}\frac{1}{x^{1/5}}}\right)^{1/4} = 0.0592\cdot\left(\frac{1}{\left(\frac{\rho U_e}{\mu}\right)^{4/5}\cdot\frac{1}{x^{1/5}}}\right)^{1/4} = \frac{0.0592}{\left(\mathrm{R}_{e_x}\right)^{1/5}}$$

Eq. 11 is integrated along the length of the port to give an averaged value for the skin friction coefficient

$$C_F = \frac{1}{L}\int_0^L \frac{0.0592}{\left(\mathrm{R}_{e_x}\right)^{1/5}} dx = \frac{0.0592}{L}\cdot\frac{1}{\left(\frac{\rho U_e}{\mu}\right)^{1/5}}\int_0^L \frac{dx}{(x)^{1/5}} = \frac{0.0592}{L}\cdot\frac{1}{\left(\frac{\rho U_e}{\mu}\right)^{1/5}}\frac{1}{4/5}\cdot L^{4/5} = 0.0592\cdot\frac{5}{4}\cdot\frac{1}{\left(\frac{\rho U_e}{\mu}\right)^{1/5}\cdot L^{4/5}} = \frac{0.074}{\left(\mathrm{R}_{e_x}\right)^{1/5}} \quad . \tag{12}$$

The resulting simple mean skin friction model is

$$C_f = \frac{.074}{\left[\mathrm{Re}_L\right]^{\frac{1}{5}}} . \tag{13}$$

The oxidizer mass flux term, $\rho_e U_e$, is related to the instantaneous cross-sectional combustion chamber area and the mass flow rate of oxidizer out of the injector with the relation

$$\rho_e U_e = \frac{\dot{m}_{ox}}{A_{c_{\text{chamber}}}} , \tag{14}$$

where, based on the oxidizer injector geometry

$$\dot{m}_{ox} = A_{ox} C_{d_{ox}} \sqrt{2\rho_{ox}(p_{ox} - p_0)} . \tag{15}$$

Substituting Eqs. 13, 14, 15 for skin friction coefficient and oxidizer mass flux into Eq. (8) derives an approximate model for the longitudinally averaged recession rate along the length of the fuel port,

$$\dot{r} = \frac{.047}{P_r^{\frac{2}{3}}\rho_{\text{fuel}}}\left(\frac{c_p\left[T_0 - T_{\text{fuel}}\right]}{h_v}\right)^{.23}\left[\frac{A_{ox}C_{d_{ox}}}{A_{c_{\text{chamber}}}}\sqrt{2\rho_{ox}(p_{ox}-p_0)}\right]^{\frac{4}{5}}\left(\frac{\mu_{ox}}{L}\right)^{\frac{1}{5}} . \tag{16}$$

The total mass flow of the fuel being generated by the regressing fuel is simply

$$\dot{m}_{fuel} = A_{burn}\cdot\rho_{fuel}\cdot\dot{r} , \tag{17}$$

As the fuel begins to burn the combustion process produces high temperature gases that escape through nozzle throat. Assuming the nozzle throat chokes immediately, the generated gases cannot escape as fast as they are produced and pressure within the fuel chamber builds. The time response of this chamber pressure growth can be calculated by a balance between the gases coming into the fuel port and the gases leaving through the choked nozzle,

$$\frac{\partial}{\partial t}M_c = \left[\dot{m}_{fuel} + \dot{m}_{ox}\right] - \dot{m}_{nozzle} . \tag{18}$$

Assuming the nozzle chokes immediately after the initiation of combustion

$$\frac{\partial}{\partial t}[\rho_c]V_c + \rho_c \frac{\partial}{\partial t}[V_c] = \left[\dot{m}_{fuel} + \dot{m}_{ox}\right] - A^* \sqrt{\frac{\gamma}{R_g}\left(\frac{2}{\gamma+1}\right)^{\frac{\gamma+1}{(\gamma-1)}}} \frac{P_0}{\sqrt{T_0}}. \tag{19}$$

Using the ideal gas law to write the density in terms of chamber pressure and substituting for the fuel mass flow using the regression equation,

$$\frac{\partial p_0}{\partial t} = \frac{A_{\text{burn}}\dot{r}}{V_c}\left[\rho_{\text{fuel}} R_g T_0 - p_0\right] - p_0\left[\frac{A^*}{V_c}\sqrt{\gamma R_g T_0\left(\frac{2}{\gamma+1}\right)^{\frac{\gamma+1}{\gamma-1}}}\right] + \frac{R_g T_0}{V_c} A_{ox} C_{d_{ox}} \sqrt{2\rho_{ox}(p_{ox} - p_0)}\,. \tag{20}$$

The growth of the port radius is described by

$$\frac{\partial R_{port}}{\partial t} = \dot{r}, \tag{21}$$

and the instantaneous chamber volume is $V_c = \pi R_{port}{}^2 \cdot L$. Equations 15, 16, 17, 20, and 21 are integrated as a system with the state vector containing combustion pressure, instantaneous combustion port radius, and the total masses of fuel and oxidizer consumed by the system. These equations allow the dynamical nature of the combustion process to be modeled as a function of time.

For a fixed oxidizer mass flow, the properties of the combustion gasses will change as the port radius grows larger and the mixture ratio becomes increasingly richer. Based on Eqs. 15, 16, and 17, it can be shown that the effective mixture ratio of the rocket is

$$M_R = \frac{\dot{m}_{ox}}{\dot{m}_{\text{fuel}}} = 21.28 P_r^{\frac{2}{3}}\left[\frac{A_{c_{\text{chamber}}}{}^{\frac{4}{5}} A_{ox}{}^{\frac{1}{5}}}{A_{burn}}\right]\frac{\left(C_{d_{ox}}\sqrt{2\rho_{ox}(p_{ox} - p_0)}\,\frac{L}{\mu_{ox}}\right)^{\frac{1}{5}}}{\left(\frac{c_p\left[T_0 - T_{\text{fuel}}\right]}{h_v}\right)^{.23}}. \tag{22}$$

For this analysis, the thermodynamic properties of the combustion products were stored as a function of chamber pressure and mixture ratio, and were evaluated at the beginning of each data frame using a two dimensional table lookup. For this analysis, the equilibrium gas-chemistry code *Chemical Equilibrium with Applications* (CEA)[11,12] was used to generate combustion properties. The CEA code was developed at NASA Glenn Research Center, and has been successfully applied for the analysis of rocket combustion, detonation, and flow across non-adiabatic shock waves. The code posits chemical reactions across the shockwave and then minimizes the Gibbs free energy[13] in order to reach thermodynamic and transport properties at chemical equilibrium. The code has extensive internal libraries for gas thermodynamic and transport properties including air at standard and non-standard conditions.

III. Experimental Data Collection

Experimental data was collected from two separate burns of a small-scale hybrid rocket motor. The motor burned a combination of nitrous oxide and hydroxyl-terminated polybutadiene (HTPB). The motor casing used for these test fires was aluminum, 1.016 meters in length and 10.2 cm in diameter. Internal to the motor casing is a PVC fuel cartridge into which was cast the solid fuel. The nozzle was manufactured from a piece of graphite. The nozzle throat diameter is 2.54 cm and has an expansion ratio of 6.452. The nozzle contour follows a partial bell, with an end plane divergence half-angle of 14 degrees. The nozzle fits internally into the fuel cartridge that fits inside the motor casing. This design allows for quick removal of both the nozzle and the fuel cartridge so that multiple grain

geometries can be tested in a single day. This motor was built and tested as partial fulfillment of the requirement for a senior design project at Utah State University.

For the test fires discussed within this report, combustion pressure, oxidizer pressure, thrust, case temperature and exhaust flame temperature were recorded. The basic test schematic can be seen in Fig. 5 and the corresponding component models can be seen in Table 1. Oxidizer pressure was measured upstream of the main oxidizer valve. Combustion pressure was measured from a port in the motor cap on the forward end of the combustion chamber. The motor was fixed to a test sled on a portable test trailer and thrust was measured at the forward end of this test sled.

Thermocouples were fastened to the outside of the motor casing and to a steel spar positioned in the exhaust plume. The thermocouple on the motor case was used to detect the presence of any abnormal temperature spikes during the burn, an indication of possible imminent burn through of the motor casing. The thermocouple situated in the exhaust plume was positioned in an attempt to gauge the exit temperature of the motor configuration before the destruction of the thermocouple.

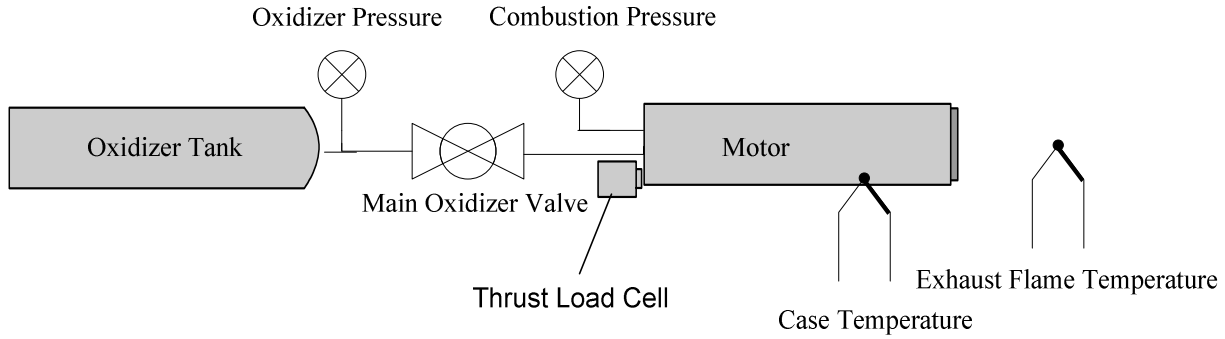

Figure 5. Test System Components

Table 1. Instrumentation System Components

Measurement	Sensor	Fieldpoint Module
Combustion Pressure	1k MSI 600 Pressure Transducer	cFP-AI118
Oxidizer Pressure	2.5k MSI 600 Pressure Transducer	cFP-AI118
Thrust	OMEGA LCCB-1K	cFP-AI118
Case Temperature	Type K Thermocouple	cFP-AI112
Exhaust Flame Temperature	Type K Thermocouple	cFP-AI112

Data acquisition was completed through the use of a National Instruments Compaq Fieldpoint. Two separate Fieldpoint modules, the cFP-AI-118 and the cFP-AI-112, were used for data collection. The 16-bit cFP-AI-118 was used to collect outputs from the MSI 600 pressure transducers and the OMEGA LLCB 1000 lbf load cell. The 16bit, lower range cFP-AI-112s were used to retrieve thermocouple voltage. The Fieldpoint system was situated on the test trailer and data was broadcast back over Ethernet to a remote, data-logging laptop. Figure 6 shows a collage of a typical test firing of a 4 inch motor including the control system arrangement.

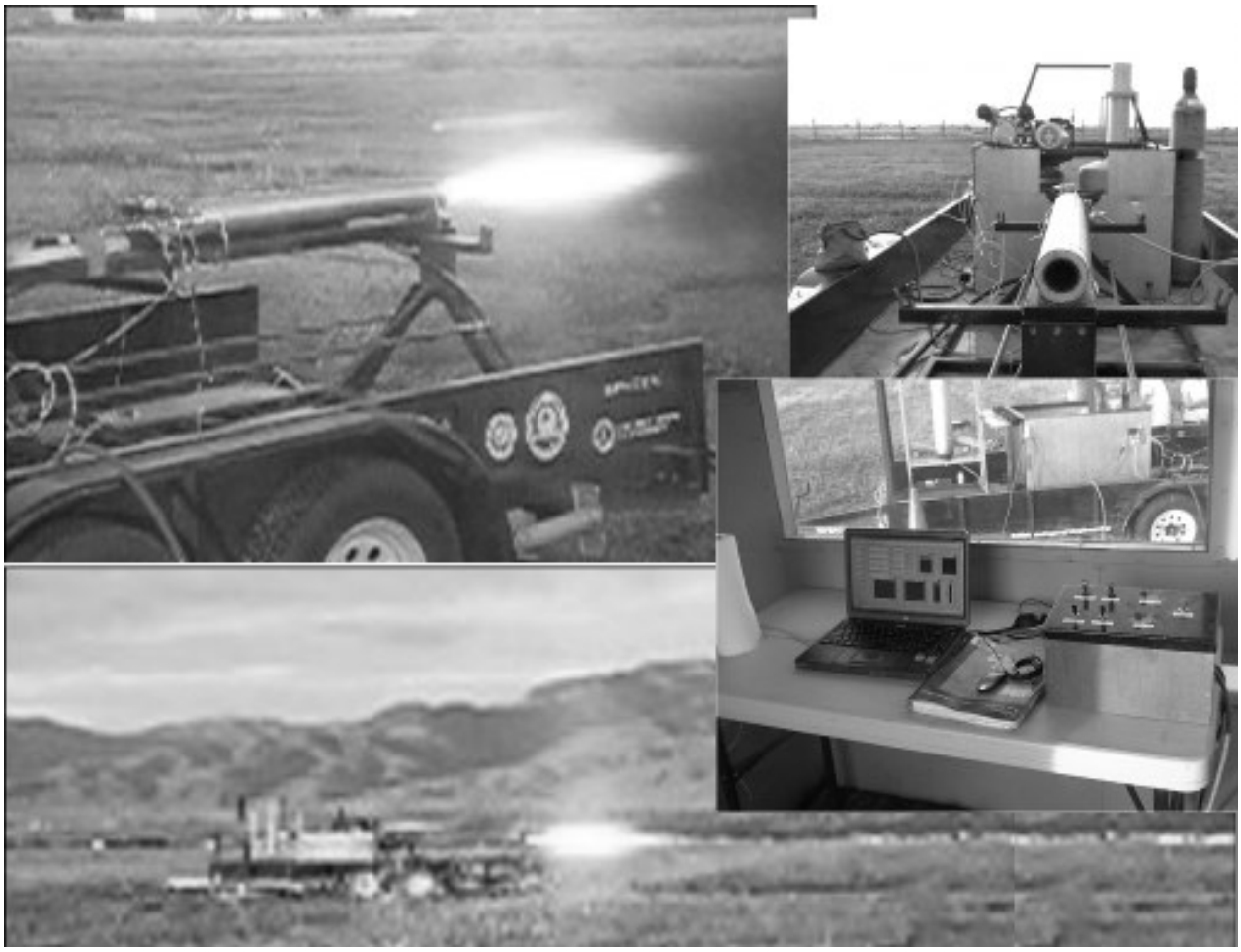

Figure 6. Typical test firing of a 4 in nitrous oxide and HTPB hybrid rocket motor.

Figure 7 shows a typical test fire data time history for oxidizer pressure (kPa), combustion pressure (kPa) and thrust (N). Upon examination of this figure, two distinct phases of combustion can be identified. The first stage is characterized by high combustion pressure and thrust. This event is a result of the upstream oxidizer being in the liquid state, resulting in a high oxidizer mass velocity and lean combustion mixture ratio. After approximately 15 seconds, the liquid nitrous oxide is consumed and combustion continues using gaseous nitrous oxide. A dramatically reduced oxidizer mass velocity and atypically rich mixture ratio during this period results in dramatically reduced thrust and chamber pressure. Combustion of this form continued for approximately another 12 seconds before the main oxidizer valve was closed, terminating combustion.

IV. Model Prediction Comparison

The first and second test fires mentioned above burned fuel grains with an initial port diameter of 2.54 cm and 5.08 cm, respectively. However, the second test fire did not yield data worthy of analysis, as it suffered a flame out shortly after ignition. Only the data from the first test fire will be discussed further. Although the regression rate model used for this analysis is longitudinally averaging, predictions from the numerical model reasonably well predict test performance in this test fire. However, before the behavior of the model could be validated, specific parameters of the relevant motor system had to be evaluated.

First, the injector discharge coefficient had to be calculated. Although the theoretical discharge coefficient was known, discrepancies due to machining irregularities and surface roughness lead to a discharge coefficient

substantially different from that estimated. This discharge coefficient was evaluated by integrating Eq. 15, the oxidizer mass flow rate for an injector, over a time logged pressure differential with a known total mass discharge. Using this method, a discharge coefficient of 0.27 was obtained for the injector. A list of the other relevant constants used for the regression rate model are shown in Table 2.

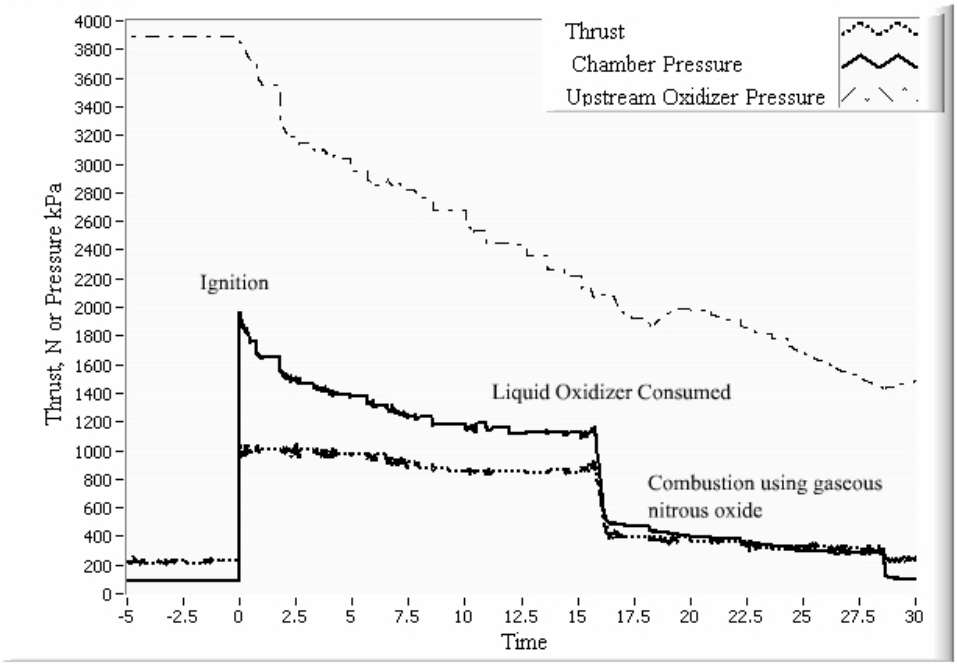

Figure 7. Time history of 4 in nitrous oxide-HTPB test fire.

Table 2. Constant Parameters for Integration Scheme

Parameter	Value
Combustion Port Length	0.8636 m
Combustion Efficiency	95.0%
Fuel Density	930.0 kg/m^3
Grain Temperature	300.0 deg K
Heat of Vaporization	1.8 MJ/Kg
Injector Area	0.35628 cm^2
Injector Discharge Coefficient	0.27
Initial Port Diameter	0.0254 m
Nozzle Throat Area	0.0005067 m^2
Nozzle Exit Divergence Angle	28.0 degrees
Nozzle Expansion Ratio	6.452
Oxidizer Liquid Density	800.0 kg/m^3

The test fires conducted for this application did not use a constant pressure system. Therefore, a decaying oxidizer pressure drove the injector pressure. This measured oxidizer pressure was imported into the motor algorithm and used to drive the upstream injector pressure. This resulted in the chamber pressure characteristics seen in Fig. 8. and the thrust characteristics seen in Fig. 9. The instantaneous mixture ratio can be seen in Fig. 10.

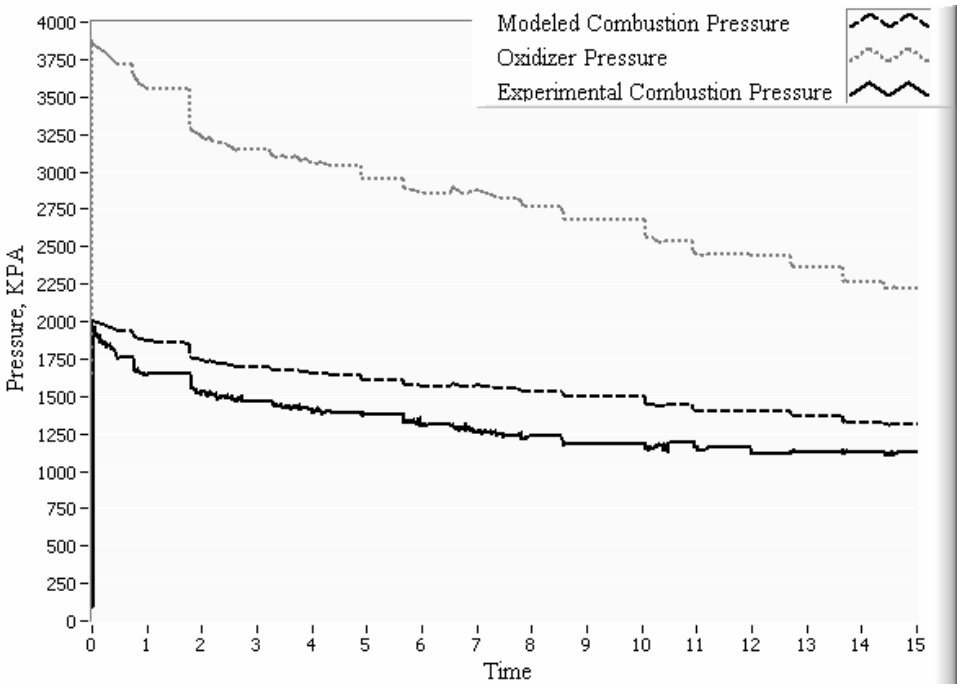

Figure 8. Oxidizer and combustion pressure from experimental results and regression rate model.

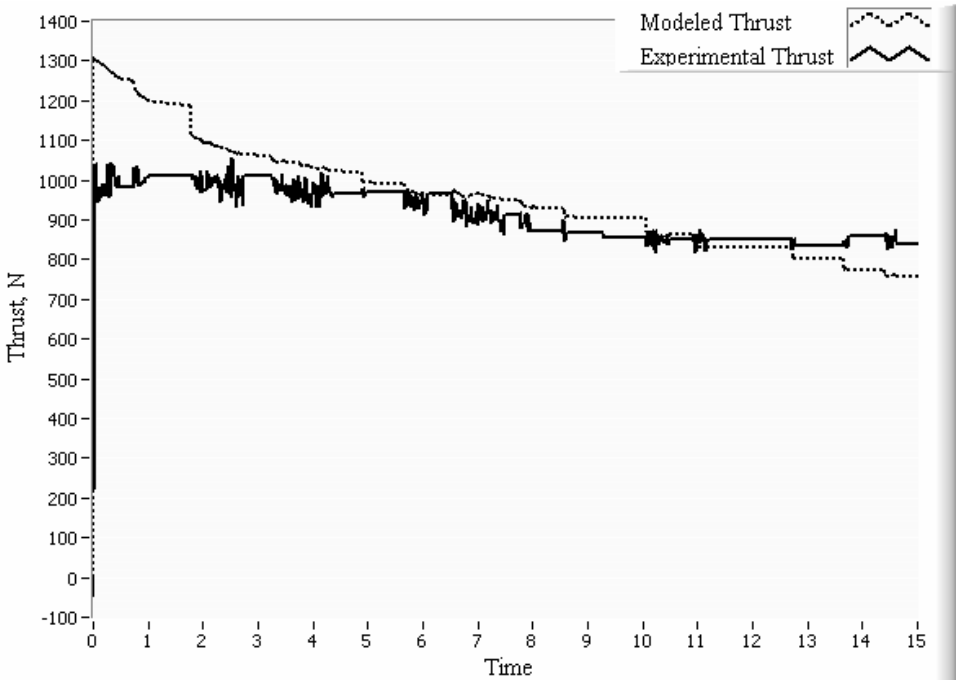

Figure 9. Thrust profile from experimental results and regression rate model.

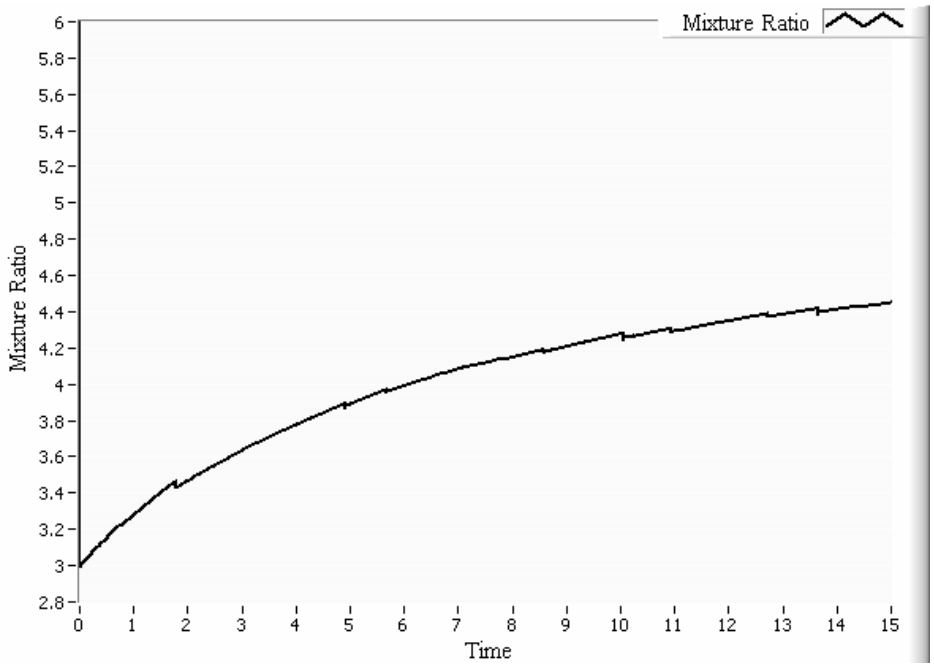

Figure 10. Mixture ratio from regression rate model.

The model, although close to experimental results, is shown to somewhat over predict combustion pressure. Correlation between the model and experimental data for thrust is very close, however, the experimental thrust profile experiences a "ramp up" not shown by the model results. This phenomenon is almost certainly due to asymmetrical burning and pitting of the fuel grain. This leads to an overall increase in surface area of the fuel grain for the later portions of the burn and, therefore, higher overall thrust.

Direct comparison of regression rates is difficult, as instantaneous regression rate sensors were unavailable at the time of the test fire. This makes it possible to correlate only a single point, the final port geometry left after the 15 second burn. However, the system tested did not have a gaseous purge, so it continued to burn, and therefore, regress, even after the liquid portion of nitrous oxide was expelled from the oxidizer tank. As the regression rate model described in this paper is only valid for nitrous oxide in a liquid state at the injector, analysis stops at this point, leading to an underestimation in the total fuel regression. The final port diameter predicted by the model was 5.93cm. The measured diameter is closer to 7.5 cm. However, considering the substantial amount of time the motor spent burning with the aid of gaseous nitrous oxide, as can be seen in Fig. 7, these results do not necessarily disagree. Integration of real-time regression rate sensing would be needed to test the validity of the total fuel regression predicted by this model.

Although the model's predicted regression rate cannot be compared to the actual regression rate data generated by the test fire, the validity of the predicted regression rate can be established by comparison to industry measured empirical data. Typically, hybrid regression rate is a function of oxidizer mass velocity raised to a constant exponent specific for the fuel and oxidizer combination. This correlation results in a linear plot when the resulting formula is plotted with respect to a logarithmic axis. As can be seen in Fig. 11, the model-predicted regression rate follows the same behavior as data generated in two test fires involving gaseous oxygen (Gox) and HTPB[14]. Considering the different oxidizers used to generate the fire data shown on Fig. 11, the model predicted regression rate shows remarkable agreement with the previously existing empirical data.

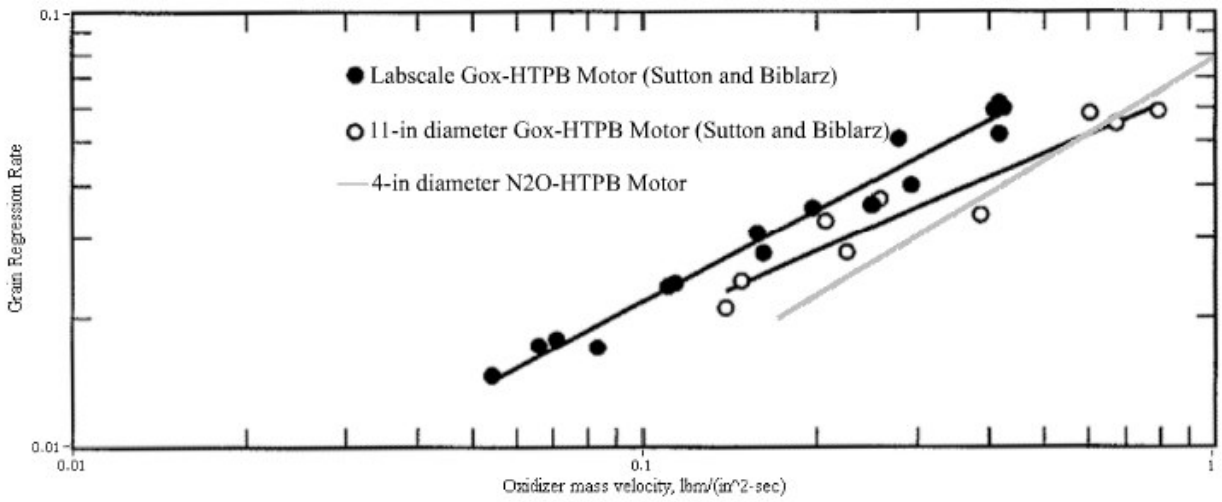

Figure 11. Empirical and modeled regression rates as a function of oxidizer mass velocity.

V. Conclusions and Future work.

This paper develops a better model for predicting the motor recession rates using an enthalpy-balance where the ablation heat of the fuel grain is balanced by the convective heat transfer from the combustion flame zone to the fuel grain surface. The recession model, based on the longitudinally averaged fuel recession rates, is shown to accurately predict the chamber pressure, thrust and specific impulse performance of small and medium scale hybrid rocket motors. The longitudinally averaged regression rate model is capable of approximately predicting the regressive characteristics and motor performance for the small scale firings analyzed in this data. However, the examination of post-burn fuel geometry for this and previous motor burns yielded the discovery of longitudinally varying regression rates and regression rate geometry. These burns have often shown deep channeling and pitting towards the aft end of the fuel grain. For a long duration burn, these channels and pits provide a significant danger to the structural integrity of the motor casing. Because of these factors, the development of a longitudinally varying regression rate model has become desirable.

Long terms goals for extending the accuracy and applicability of the regression model are

1) Develop a platform for rapidly testing small to medium scale motor, and the system must be capable of capable of retrieving regression rate correlations to refine design models,
2) Perform multiple static test fires of the motor over a variety of fuel grain designs, including propellant burn enhancements.
3) Use these test data to modify and calibrate design models, and extend codes from axi-symmetric, longitudinal mean predictions to three-dimensional models.

References

[1] I-Shing Chang, "Investigation of Space Launch Vehicle Catastrophic Failure," AIAA Paper, July 1995. (AIAA 95-3128).

[2] U.S. Department of Transportation, " Hazard Analysis of Commercial Space Transportation," May 1988.

[3] Biblarz, O., and Sutton, G. P., *Rocket Propulsion Elements*, John Wiley and Sons, New York, 2001, p. 10.

[4] Cheng, C. G., Farmer, R. C., Jones, H. S., and McFarlane, J., S., Numerical simulation of the internal ballistics of a hybrid rocket, AIAA Paper # 94-0554, 1994.

[5] Chiaverini, M. J., Kuo, K., K., Peretz, A., and Harting, G., Regression-Rate and Heat-Transfer Correlations for Hybrid Rocket Combustion, Journal of Propulsion and Power, Vol. 17, No. 1, January-February 2001.

[6] Biblarz, O., and Sutton, G. P., *Rocket Propulsion Elements*, John Wiley and Sons, New York, 2001, pp. 733.

[7] [1]White, Frank M., *Viscous Fluid Flow*, McGrawHill, Inc., New York, 1991, pp. 485-486.

[8] [3]Crawford, M. E., and Kays, W. M., *Convective Heat and Mass Transfer*, McGraw-Hill, New York, 1993, pp. 260.

[9] Lees, L., "Convective Heat Transfer with Mass Addition and Chemical Reactions," *Combustion and Propulsion, 3rd AGARD Colloquium*, New York, Pergamon Press, 1958, p. 451.

[10] White, Frank M., Viscous Fluid Flow, McGrawHill, Inc., New York, 1991, pp. 429-430.

[11] Gordon, S., and McBride, B. J., "Computer Program for Calculation of Complex Chemical Equilibrium Compositions and Applications", NASA RP-1311, 1994.

[12] Gordon, S., and McBride, B. J., "Computer Program for Calculation of Complex Chemical Equilibrium Compositions and Applications, Vol. 2, Users Manual and Program Descriptions", NASA RP-1311, 1994.

[13] Zeleznik, F. J., and Gordon, S., "Calculation of Complex Chemical Equilibria", *Journal of Industrial and Engineering Chemistry*, vol. 60, no., 6, pp. 27-57.

[14] Biblarz, O., and Sutton, G. P., *Rocket Propulsion Elements*, John Wiley and Sons, New York, 2001, 591-592.